

Experimental Seismic Performance of a Reduce-Scale Stone Masonry Loess Cave With Traditional Buildings

Xiangbi Zhao (✉ zhaoxiang0711@163.com)

Yulin University <https://orcid.org/0000-0002-2701-0538>

Jiayang Xue

Xi'an University of Architecture and Technology

Fengliang Zhang

Xi'an University of Architecture and Technology

Research Article

Keywords: SMLC, shaking table test, seismic response, torsion angle, damage level

Posted Date: September 29th, 2021

DOI: <https://doi.org/10.21203/rs.3.rs-928122/v1>

License:   This work is licensed under a Creative Commons Attribution 4.0 International License. [Read Full License](#)

Version of Record: A version of this preprint was published at Bulletin of Earthquake Engineering on April 19th, 2022. See the published version at <https://doi.org/10.1007/s10518-022-01380-5>.

Abstract

The seismic behavior of the independent type of a stone masonry loess cave (SMLC) is examined. A tri-directional shake table test was employed on 1:4 reduced-scale specimen of SMLC. The specimen represented a typical traditional dwelling of the loess region in China, consisting of unreinforced masonry walls and inner loess, without any seismic treatment. The dynamic parameters directly measured by the test include the acceleration response, displacement response of each key position of the stone masonry loess cave, and the detailed record of the damage form of the structure under each loading. The analysis results indicated that the simplified model design method not only satisfied the main similarity relationship of the reduced-scale structure shaking table test, but also achieved excellent test results. Through the calculation results to determine the torsion angle of the node and the deformation between the layers, corresponding strengthening measures could be proposed for the life extension protection of this traditional building. Finally, according to the analysis of the test results, the damage state and damage level of the prototype of the SMLC is established.

1. Introduction

Masonry (stone) has been widely used as a building material in various parts of the world. Stones are ubiquitous all over the world, and most of them have high strength. As a historic building material, its advantages are low cost, easy to obtain, and durable (Siegesmund et al. 2011; Hendry et al. 2001). The stone building is usually a composite structure composed of stone, cementitious material (mortar), and the backfilling material between the walls (Krzan et al. 2015). Due to the diversity of materials and shapes of natural stones, the types of stone buildings around the world are varied (Krzan et al. 2015). In recent years, some experts have noticed the problem of anti-seismic protection of ancient buildings (Zhao et al. 2019; Xie et al. 2019; Xie et al. 2020a; Xie et al. 2020b; Poletti et al. 2015; Aktas et al. 2016). As the historical stone buildings have not fully considered the seismic performance of the structure, the stone buildings have performed poorly in the past earthquakes, showing a high degree of vulnerability (Rovero et al. 2016; D'Ayala et al. 2011; Carocci 2012; Lagomarsino et al. 2013). At home and abroad, experimental research, mechanical model analysis, and numerical simulation analysis of stone masonry buildings show that various parameters of the structure have a significant influence on the stiffness, strength, deformability, and bearing capacity. In addition to the parameter characteristics of the primary constituent materials, stone, mortar, and infilling materials, they are also affected by the geometry of the structure, the static and dynamic boundary conditions applied to the stone masonry structure, the type of test and other factors (Krzan et al. 2015; Zhang et al. 2019; Silva et al. 2014; Milosevic et al. 2013; Zhang et al. 2018). In the laboratory, the specimen (prototype reduced scale) is built on the ground beam and loaded, so there is still a deviation between the obtained test results and the prototype, which is also an essential factor for the accuracy of the test results (Corradi et al. 2018).

Stone masonry loess cave (SMLC) is unique to the loess area of northwestern in China (Fig. 1) and are widely distributed in Shaanxi, Shaanxi, Henan, Gansu and other provinces (Ballard et al. 1967; Yu et al. 2009; Zhu et al. 2014). Most of the sites where SMLCs are located are marginal mountainous areas with difficult living conditions, and their construction is concentrated in a period when the processing industry is very backward. Therefore, most of the stones used in the construction of the cave are natural and raw rock, with different shapes and very uneven sizes. Generally, the maximum length of the stone is less than 2/3 of the thickness of the stone cave.

According to the classification in the masonry building database, SMLC is rubble stone masonry walls (containing other infilling materials and irregular masonry (MIT 2009)), which are usually called A-typology masonry. Still, there are few data on this research (Krzan et al. 2015). Due to the no lateral connections member, the poor properties of cementitious materials, and the lack of detailed design of the joints, this type of masonry structure has the highest risk

of damage in or out of the plane (Corradi et al. 2018; Borri et al. 2015). Therefore, it was necessary to profoundly study the influence parameters of the seismic response performance of such a stone structure under the action of earthquake and evaluate the seismic performance of the building.

Scholars have always maintained a keen interest in the seismic performance of the masonry structure that has a commemorative or even for thousands of years. The interesting point is that for this type of building without aseismic treatment, how to not collapse still after many earthquakes in service. Extensive research has been carried out on the seismic performance of the masonry structure. Since many masonry buildings which have commemorative significance have been protected, destructive research cannot be conducted. In the study of seismic performance, the scholars used in-situ dynamic penetration technology or built an overall reduced scale model to carry out shaking table test, and analyzed the seismic performance of these unique structures (Cakir et al. 2016; Colapietro et al. 2013; Bennati et al. 2015). And according to the test results, the seismic evaluation method for stone masonry buildings was established (Cakir et al. 2016; Preciado 2015). These studies have shown that the stone masonry structures are particularly vulnerable to earthquake damage. Through the finite element analysis method, excellent results had been achieved in the seismic performance analysis of stone masonry structure (Preciado 2015; Valente et al. 2016; Preciado et al. 2019). Especially in Europe, where the stone building is widely used, people have conducted a large number of tests on free-standing stone buildings with European characteristics and gained generous valuable research experience (Tomažević et al. 1991; Magenes et al. 2014; Senaldi et al. 2018; Vintzileou et al. 2015; Mouzakis et al. 2018; Graziotti et al. 2017; Tomassetti et al. 2017). After many major earthquakes, due to the occurrence of heavy casualties, many experts had noticed this unique type of building (loess cave) in Northwest China, so had begun to study the seismic performance (Costa et al. 2012). Among them, Xue et al. (2020) and Zhao et al. (2020, 2021) conducted some comprehensive study on the seismic performance of loess cave composed by raw soil materials and obtained fruitful results. However, in recent, no relevant research on stone masonry loess cave has been found.

In this study, the seismic performance of SMLC buildings with Chinese traditional architecture characteristics was studied. To this end, a large-scale shaking table test was carried out at the Xi'an University of Architecture and Technology (XAUAT) for the SMLC specimen with a 1:4 scale ratio, and the indoor building material performance tests were conducted on the primary building materials. The main purpose of this study was to generate new experimental data on the dynamic behavior of SMLC under earthquake action, which could contribute to enrich the database of stone masonry buildings and evaluate the seismic performance of existing stone masonry buildings. The general seismic response characteristics of prototype SMLC are discussed, and the seismic performance of SMLC was assessed by combining engineering demand parameters and energy limit states.

2. Test Procedure

2.1 Prototype situation

The members of the research group went to Shaanxi, Shanxi, Henan, and other provinces for 696 SMLC buildings to conduct a survey. The survey content mainly included necessary information such as structure, size, and survival status, and the results are shown in Table 1. Because the primary materials (stone materials) used in SMLC were obtained locally, the size of SMLC was closely related to the size, quality, and strength of stone. To study the seismic characteristics of the existing SMLC structure, the most typical triple-hole free-standing stone cave in Shanxi Province was used as a prototype. The detailed dimensions are shown in Table 2. According to the survey results of SMLC in Shanxi, it was found that 31% of the stone cave was in the 8-degree fortification zone, 52% of the stone cave was in the 7-degree fortification zone, and 17% of the stone kilns were in the 6-degree fortification zone. At the same time, there was no difference in the construction scale, size, and material performance of these stone cave. Therefore,

seismic performance analysis was required for stone caves at 7 and 8 degrees of fortification. According to China's seismic design specifications GB 50011 – 2010 “Code for seismic design of buildings” (GB 2016), the seismic fortification intensity at the location of the prototype was 7 degree (8 degree), the design basic earthquake acceleration was 0.10 g (0.20 g), and the classification of design earthquake all set as second.

Table 1 Survey results of dimension of stone masonry loess cave (unit: m)

Province	Arch type	Number	Width of cave	Height of cave leg	Width of internal wall	Width of external wall	Vector height	Building height	Depth of cave	Thickness of covering
Shaanxi	Circle	40	2.5-4.0	1.5-2.5	0.6-1.0	0.8-3.4	1.0-2.0	2.8-3.5	5-20	0.5-2.0
	Other	112	2.3-4.4	1.5-2.5	0.5-1.5	0.7-3.8	1.0-2.5	3.0-5.0	6-25	0.5-2.5
Shanxi	Circle	67	2.5-3.8	1.6-2.2	0.5-1.0	1.0-3.0	1.2-2.0	2.5-3.8	10-20	0.7-1.8
	Other	168	2.4-5.1	1.6-2.3	0.5-1.2	1.0-3.5	1.0-2.5	2.6-4.4	8-30	0.4-2.3
Henan	Circle	55	2.8-4.2	1.8-2.4	0.7-1.5	0.9-3.0	1.1-2.1	3.2-4.5	10-25	0.8-2.5
	Other	154	3.0-5.6	1.4-2.5	0.6-1.6	0.8-3.4	1.0-2.4	3.0-5.0	10-30	0.7-2.8
Hebei	Circle	32	3.2-4.8	1.6-2.3	0.5-1.5	1.0-3.5	1.2-2.2	3.5-4.5	15-26	0.8-2.4
	Other	68	2.6-4.2	1.5-2.5	0.4-1.8	0.8-3.0	1.1-2.8	3.0-4.6	9-20	0.5-2.8

Table 2 Size of prototype and specimen (unit: m)

Parameter	Width of cave	Height of cave leg	Vector height	Width of external wall	Width of internal wall	Thickness of covering	Depth of cave	Arch thickness
Prototype	3	1.8	1.5	1.2	0.6	1.2	6.6	0.3
Specimen	0.75	0.45	0.375	0.30	0.15	0.30	1.65	0.075

2.2 Scaling factors

This test was conducted in the laboratory of Xi'an University of Architecture and Technology. Due to the limited performance conditions of the laboratory device, this test uses a shrinkage scale model with a lack artificial mass (Vintzileou et al. 2015; Mouzakis et al. 2018). According to the size of the selected prototype in the research and the size of shaking table, the length scale of the stone cave was set to 1:4 (the detailed dimensions of the specimen are shown in Table 2), and after ensuring that the similarity ratio of elastic modulus and strain were 1:1, increasing reasonable artificial counterweight, determining the acceleration similarity constant 2:1, and obtaining the other similarity ratio according to the dimensional analysis method (Table 3) (Vintzileou et al. 2015; Mouzakis et al. 2018). Since the dynamic characteristic parameters such as the time similarity ratio of the specimen were not 1:1, the

parameters of the seismic input in the test also need to be adjusted accordingly. According to a similar relationship, the part of the infilled loess and the external masonry structure of the test specimen required to add artificial counterweight, respectively.

Table 3 Similarity ratio on shaking table test

Features	Parameter	Relationship	Similarity ratio
Geometric features	Length (l)	C_l	1:2 ²
	Displacement (δ)	C_δ	1:2 ²
Material features	Stress (ε)	C_ε	1:1
	Strain (σ)	$C_\sigma = C_E \cdot C_\varepsilon$	1:1
	Elastic modulus (E)	C_E	1:1
	Mass (m)	$C_m = C_\sigma \cdot C_l^2 / C_a$	1:2 ⁵
Dynamic features	Time (t)	$C_t = (C_l / C_a)^{0.5}$	1:2 ^{1.5}
	Acceleration (a)	$C_a = C_l / C_t^2$	1:2 ⁻¹
	Frequency (f)	$C_f = 1 / C_t$	1:2 ^{-1.5}
	Damping (ξ)	$C_\xi = C_E \cdot C_l \cdot C_t / C_a$	1:2 ^{4.5}

2.4 Determination of material properties of the SMLC

SMLC was composed of three materials, including stone, mortar, and loess. The arches and walls were consisted of stone and mortar and formed a groove shape structure. Additionally, infilled loess material was used in the groove shape structure by arches and walls. The cave structure was supported on firm ground. In this study, the properties of SMLC materials were defined by comprehensive material tests.

2.4.1 Stone material

According to the relevant provisions of China's "Code for Design of Masonry Structures" (GB 50003 – 2011) (GB 2011), the same stone samples as the prototype SMLCs were selected, and the stones were divided into four groups of 12 cube test pieces with the length of 70 mm. The compressive strength test was carried out on a 200 ton hydraulic testing machine. The test results of the compressive strength of the stones are shown in Table 4, and the results of Table 4 are plotted in Fig. 2. These indicated that the compressive strength of the stones presented a discrete type, and most of its compressive strength exceeded 100 MPa. Granite with high strength was mainly selected for the construction of SMLC materials, and there were random micro-cracks in the granite itself, which led to the randomness of the compressive strength and the dispersion of the compressive strength of the stones (Vasconcelos et al. 2009).

Table 4 Compressive strength of stone

Group No.	Sample No.	Cross section (mm ²)	Peak force (kN)	Compressive strength (MPa)	Mean compressive strength (MPa)
A	1	70 × 70	524.3	107	104.25
	2		519.4	106	
	3		450.8	113	
B	4		553.7	92	
	5		485.1	99	
	6		465.5	95	
C	7		543.9	103	
	8		504.7	103	
	9		509.6	104	
D	10		504.7	111	
	11		529.2	108	
	12		539	110	

According to "Standard for test methods of Engineering Rock Mass" (GB/T 50266-2013) (GB/T 2013), one of the four groups of stone specimens was selected for uniaxial compression deformation test to determine strain value of the axial and the radial, calculation the elastic modulus and Poisson's ratio of the rock according to Table 5.

Table 5 Modulus of elasticity and Poisson's ratio of stone

Group No.	Ultimate compressive strength (MPa)	Elasticity modulus (GPa)	Poisson's ratio	Axial peak strain $\mu\epsilon$	Transverse peak strain $\mu\epsilon$
A	108	49.5	0.26	1404	365
B	100	48.2	0.28	1511	423
C	104	44.3	0.30	1556	467
D	110	47.5	0.28	1387	388
Mean	105.5	47.4	0.28	1464.5	410.8

2.4.2 Mortar

According to Chinese code (JGJ/T 136–2017) "Technical Specification for Testing the Compressive Strength of Masonry Mortar by Penetration Method Resistance Method" (JGJ/T 2017), the compressive strength of the mortar obtained through in-situ field test on the cemented materials of the SMLC prototype was 4.5 MPa. For the mortar performance of specimen close to the prototype, the material properties of the mortar test sample with trial mix ratio were tested according to "Standard for Test Method of Performance on Building Mortar" (JGJ/T70-2009) (JGJ/T 2009), and the test results are shown in Table 6. Finally, the mass ratio of the mortar used in this test was determined as follows: cement: sand: water: white ash = 1: 4.24: 0.83: 0.3, and the compressive strength of the mortar test

samples was 4.45 MPa. Due to the non-uniformity of the SMLC, there was no specific requirement for the thickness of the mortar ash joint, and it only needed to make the mortar full during the masonry process and facilitate the construction.

Table 6 Compressive strength of mortar

Mortar sample No.	M1	M2	M3	M4	M5	M6	Mean
Failure force (kN)	22.2	20.4	20.7	18.8	27.3	22.1	21.92
Compressive strength f_m' (MPa)	4.9	4.1	4.1	3.7	5.5	4.4	4.5

2.4.3 Masonry units

The external walls and arches of the SMLC were the composite material composed of stone and mortar. Therefore, the composite material homogeneity theory can be used to obtain the material properties of the masonry unit. Based on the compressive strength gained in the previous material properties tests for stone and mortar, an empirical formula for masonry units is (Proske et al. 2009),

$$f_{c,mas} = a f_{c,st}^b f_{c,mo}^c \quad (1)$$

where $f_{c,mas}$ represents compressive strength of homogenized masonry unit, a represents classification coefficient of the masonry unit. b and c represent coefficients, depending on the volumetric ratio of stone and mortar, respectively.

For the correlation coefficient in Eq. (1), Ril 805 (Ril 1999) gives the recommended value.

$$f_{c,mas} = 0.8 f_{c,st}^{0.70} f_{c,mo}^{0.20} \quad (2)$$

where $f_{t,mas}$ represents a tensile strength of masonry units, and usually take $0.1 \cdot f_{c,mas}$ (Kahraman et al. 2012).

The calculation formula of Poisson ratio ν_{mas} and density γ_{mas} of masonry units are (Ersoy HY 2001),

$$\gamma_{mas} = \gamma_{st} V_{st} + \gamma_m V_m \quad (3)$$

$$\nu_{mas} = \nu_{st} V_{st} + \nu_m V_m \quad (4)$$

where V_{st} represents the volumetric ratio of stone, and V_m represents the volumetric ratio of mortar. Elasticity modulus E_{mas} of masonry unit is taken as $E_{mas} = 1000 \cdot f_{c,mas}$ (ENV 2005). Homogenized material properties, volumetric ratios of stone, and mortar of masonry units were shown in Table 7 (Pelà et al. 2013).

Table 7 Homogenized material properties of masonry units

Material properties	Arches	Walls
V_{st}/V_m	0.91/0.09	0.88/0.12
$f_{c,mas}$ (MPa)	8.62	7.98
$f_{t,mas}$ (MPa)	0.86	0.80
E_{mas} (MPa)	9200.1	8420.2
ρ_{mas} (ton/m ³)	2.61	2.34
u_{mas}	0.27	0.27

2.4.4 Infilled loess

It is well known that the necessary condition for the formation and stability of the arch structure is that the upper part of the arch has sufficient vertical pressure, so the performance of the loess filling in the groove structure formed by the external wall and arch in the SMLC has a significant influence on the force of the upper part of the stone masonry arch. When the specimen was produced, the consistency of the performance indexed of the infilled loess in the specimen and the consistency of the loess material in the prototype structure must be strictly controlled, so that the selected similarity ratio and the application of artificial weights had scientific significance. And to ensure that the specimen had higher accuracy in reflecting the seismic performance of the prototype structure under the earthquake action. The undisturbed soil samples of the masonry cave prototype covering were selected for the material property test, and the results are shown in Table 8.

Figure 8 Material test results of infilled loess

Material	Water content w	Specific gravity G_s	Density ρ	Dry density P_d	Compression Modulus E_s	Cohesion c	Angle of internal friction φ
	(%)	-	[g/cm ³]	[g/cm ³]	[MPa]	(kPa)	(°)
Loess	11.60	2.71	1.82	1.63	5.44	64.22	29.29

2.5 Mass

According to the acceleration similarity ratio of 2:1, and after several pulsation tests to adjust, the weight of the artificial counterweight was finally determined. Since the external walls of the stone cave and the infilled loess needed to add corresponding artificial counterweights, in order to accurately apply the counterweight to the relevant positions, a steel frame as an intermediary between the artificial counterweight and the structure was designed to transmit force. The internal grid and bottom vacant of the steel frame were used to place the weight block, and the mass of the weight block was applied to the upper surface of the loess covering; the reinforced concrete weight block was set to above of steel frame, and the gravity of counter-weight was transferred to the stone external walls by the steel frame. The four sides of the steel frame were fixed on the top of the stone cave specimen with channel steel. The concrete counterweight was placed in the angle steel channel welded on the steel frame in advance, and the steel frame and the concrete were fixed with flower basket bolts, steel strands, and glass glue. According to the calculation results of the similarity ratio and material test of the masonry material and the loess material, it could be seen that the infilled loess part needs to increase the counterweight by 4.0 ton, and the stone masonry part required to increase the counterweight

by 3.6 ton. The 4.0 ton lead weight block on the infilled loess material was placed in the gap of the steel frame and fixed with foam glue. The weight of the external masonry wall was 3.0 ton reinforced concrete weight block plus the steel frame weight 0.6 ton.

2.6 Construction details

The stone used in the face part of the common SMLC is mostly dressed stone, with large size and exquisite processing. On the one hand, the cave looks beautiful and clean; on the other hand, it could improve the stability and bearing ability of the front facade. However, if used the same facade treatment when making the specimen, the destruction form of the cave would not be accurately obtained. Therefore, when constructed the specimen of SMLC, the same model was used for the facade and the main body of the cave. The major difference between Chinese SMLC and arched stone masonry buildings abroad was that the interior was filled with rammed loess (e.g., in European countries, the construction material at the external wall and its internal infilled material all are stone). Therefore, the construction was mainly divided into two stages: the first was the masonry of the outer wall and arch, and the second was filled with loess material. The whole construction process is shown in Fig. 3. Among them, in the process of covering infilling, the loess material would be layered and rammed in layers of every 100 mm (referred to the performance indicators of the prototype loess material and determined according to test rammed). After the covering loess was filled, it was covered with polyethylene film to prevent the rapid evaporation of water in the loess and cause the loess to crack. Then it could stand for three months and waited for the loess to consolidate.

2.7 Instrumentation and load device

The main loading equipment used in this research on the seismic performance of SMLC was a large three-dimensional, six-degree-of-freedom shaking table produced by the MTS company. Due to the limitation of the number of channels of the signal collection device, a maximum of 12 high-precision displacement meters could be set to key part of SMLC. According to the principle of symmetrical layout, the displacement meters were arranged at the free boundary with a large seismic response in the west side cave and the west side of the middle cave to obtain the displacement response of the structure under the action of simulated earthquakes. Three displacement meters were arranged at ± 0 m, in order to the input displacement of the structure was measured. Besides, because the SMLC often produces roof fall, the displacement meters in the z-direction was installed at the vault of the middle cave and side cave to measure the vertical displacement response of the vaults under the earthquake action. A total of 27 accelerometers (three accelerometers were arranged at ± 0 m to obtain input acceleration) were installed on the east cave and middle cave, in order to measure the acceleration response of the critical parts of the stone cave. The detailed arrangement of displacement and acceleration sensors is shown in Fig. 4.

2.8 Test protocol

Two natural waves and one fitted artificial wave (Short for AR) were selected according to the structural properties and site characteristics of the stone cave structural prototype, and El Centro (Short for EL) and LA-Hollywood wave (Short for LA) were selected in the natural wave (Fig. 5). The X-direction was the main seismic direction, and the same input earthquake waveform was used for three seismic directions. The input acceleration of three earthquake waves conformed to the ratio of the X-direction: Y-direction: Z-direction = 1:0.85:0.65. The response spectrum curves of the three input seismic waves and seismic codes are shown in Fig. 5(d). It was indicated that all three seismic waves could be suitably used as seismic excitations of an independent stone cave under the action of earthquakes. Table 9 lists the nominal (target) peak ground acceleration (short for PGA).

Table 9 Test procedure

No.	Condition	Earthquake excitation	PGA (g)			Seismic level
			X dir.	Y dir.	Z dir.	
1	WN-0	White noise	0.05	0.05	0.05	Frequent earthquake of 7 degree
2	EL-x1	El Centro	0.07	-	-	
3	LA-x1	LA - Hollywood	0.07	-	-	
4	RG-x1	Artificial	0.07	-	-	
5	EL-y1	El Centro	-	0.07	-	
6	LA-y1	LA - Hollywood	-	0.07	-	
7	RG-y1	Artificial	-	0.07	-	
8	EL-xy1	El Centro	0.07	0.0595	-	
9	LA-xy1	LA - Hollywood	0.07	0.0595	-	
10	RG-xy1	Artificial	0.07	0.0595	-	
11	EL-xyz1	El Centro	0.07	0.0595	0.0455	
12	LA-xyz1	LA - Hollywood	0.07	0.0595	0.0455	
13	RG-xyz1	Artificial	0.07	0.0595	0.0455	
14	WN-1	White noise	0.05	0.05	0.05	
15	EL-x2	El Centro	0.14	-	-	Frequent earthquake of 8 degree
16	LA-x2	LA - Hollywood	0.14	-	-	
17	RG-x2	Artificial	0.14	-	-	
18	EL-y2	El Centro	-	0.14	-	
19	LA-y2	LA - Hollywood	-	0.14	-	
20	RG-y2	Artificial	-	0.14	-	
21	EL-xy2	El Centro	0.14	0.119	-	
22	LA-xy2	LA - Hollywood	0.14	0.119	-	
23	RG-xy2	Artificial	0.14	0.119	-	
24	EL-xyz2	El Centro	0.14	0.119	0.091	
25	LA-xyz2	LA - Hollywood	0.14	0.119	0.091	
26	RG-xyz2	Artificial	0.14	0.119	0.091	
27	WN-2	White noise	0.05	0.05	0.05	
28	EL-x3	El Centro	0.20	-	-	Fortification earthquake of 7 degree
29	LA-x3	LA - Hollywood	0.20	-	-	
30	RG-x3	Artificial	0.20	-	-	

31	EL-y3	El Centro	-	0.20	-	
32	LA-y3	LA - Hollywood	-	0.20	-	
33	RG-y3	Artificial	-	0.20	-	
34	EL-xy3	El Centro	0.20	0.17	-	
35	LA-xy3	LA - Hollywood	0.20	0.17	-	
36	RG-xy3	Artificial	0.20	0.17	-	
37	EL-xyz3	El Centro	0.20	0.17	0.13	
38	LA-xyz3	LA - Hollywood	0.20	0.17	0.13	
39	RG-xyz3	Artificial	0.20	0.17	0.13	
40	WN-3	White noise	0.05	0.05	0.05	
41	EL-x4	El Centro	0.44	-	-	Rare earthquake of 7 degree and fortification earthquake of 8 degree
42	LA-x4	LA - Hollywood	0.44	-	-	
43	RG-x4	Artificial	0.44	-	-	
44	EL-y4	El Centro	-	0.44	-	
45	LA-y4	LA - Hollywood	-	0.44	-	
46	RG-y4	Artificial	-	0.44	-	
47	EL-xy4	El Centro	0.44	0.374	-	
48	LA-xy4	LA - Hollywood	0.44	0.374	-	
49	RG-xy4	Artificial	0.44	0.374	-	
50	EL-xyz4	El Centro	0.44	0.374	0.286	
51	LA-xyz4	LA - Hollywood	0.44	0.374	0.286	
52	RG-xyz4	Artificial	0.44	0.374	0.286	
53	WN-4	White noise	0.05	0.05	0.05	
54	EL-x5	El Centro	0.6	-	-	Between fortification and rare earthquake of 8 degree
55	EL-y5	El Centro	-	0.6	-	
56	EL-xy5	El Centro	0.6	0.51	-	
57	EL-xyz5	El Centro	0.6	0.51	0.39	
58	WN-5	White noise	0.05	0.05	0.05	
59	EL-x6	El Centro	0.8	-	-	Rare earthquake of 8 degree
60	EL-y6	El Centro	-	0.8	-	
61	EL-xy6	El Centro	0.8	0.68	-	
62	EL-xyz6	El Centro	0.8	0.68	0.52	
63	WN-6	White noise	0.05	0.05	0.05	

Note: The seismic inputs are loaded in the order of working conditions until the specimen is severely damaged or it is not appropriate to continue loading. Two-way and three-way loading are carried out according to the ratio of X:Y=1:0.85 and X:Y:Z=1:0.85:0.65 respectively.

3 Test Analysis

3.1 Damage evolution

After each seismic loading, the structural damage status of SMLC was investigated in detail. As shown in Fig. 6, the cracks were accurately drawn, showing the evolution of the damage pattern on each facade. New cracks appeared after each load was marked in red, while those that have appeared in previously loadings are indicated in black.

When the structure was at PGA = 0.14 g (DS1), the model was dominated by rigid body movement, no visible deformation and cracks appear, and the overall structure was still in the stage of elastic deformation. When PGA = 0.20 g (DS2), slight damage occurred in the local area of the specimen, and some hairline cracks appeared on the upper and lower ends of the wall on both sides of the east and west. PGA increased to 0.44 g, hairline cracks appeared in many places in the specimen, but the overall performance was excellent, and the main body of the cave was in the elastoplastic stage. Entering PGA = 0.60 g (DS3), the cracks at the vault of the cave continue developed, and the damage to the structure was intensified in most places. The cracks at the connection between the middle cave leg and the foundation were connected, and the maximum width reached 0.5 mm. Entering PGA = 0.80 g (DS4), cracks were formed at the connection between the middle cave leg and the foundation, and at the same time, the crack at the cave face extended into the hole (width 1-2.2 mm) until the back wall. Roof fall appeared in the structure was on the verge of collapse. The damage evolution mechanism of the SMLC structure and the controlled facade of each damage level are shown in Table 10.

Table 10
Summary table of damage limit states for the building specimen

Facade	DL1	DL2	DL3	DL4
North wall	No visible damage	<p>At a distance of 300 mm from the bottom of the wall and 450 mm from the east edge, a 30 mm long horizontal hairline crack appeared.</p> <p>At a distance of 800 mm from the bottom of the wall, a 100 mm long horizontal crack appeared.</p> <p>At a distance of 500 mm from the west edge, a radial crack extending upwards appeared at the bottom of the wall.</p>	<p>Cracks appeared at the bottom of the wall and extended 600mm to the west.</p> <p>The upper part of the wall is 150mm away from the west edge, and a vertical crack of 400mm in length appears and is connected with the horizontal crack on the lower side.</p> <p>At a distance of 500mm from the bottom of the wall and 500mm from the east edge, a 350mm vertical crack appeared and was connected to the upper crack.</p>	<p>The bottom crack develops diagonally upwards and connects with the crack in the northwest corner of the kiln roof, forming a through crack.</p> <p>There are two upward cracks in the middle of the east side of the wall, one diagonally to the west connects the legs of the east middle cave, and the other extends vertically up to the cave top, and the width is close to 5mm.</p> <p>There are many cracks in the middle of the wall extending to the bottom of the wall, all of which are penetrating cracks.</p>
South wall	Hairline cracks at cave top	<p>On the cave top on the west side cave, vertical hairline cracks appeared.</p> <p>At the entrance of the cave on the west side cave, a 130 mm long diagonal crack appeared and extended into the inner cave.</p> <p>A small crack of 38-50mm in length appeared on the bottom of the middle legs of both sides.</p>	<p>The crack on the west side cave top extends down to the vault, and the width of the crack on the upper part extends to 13mm.</p> <p>On the vault of the east side cave, diagonal cracks appeared and upward extended to the cave top.</p> <p>At the joint between the arch and the middle leg on the east side cave, a horizontal penetration crack appeared, extending 550mm to inner cave.</p> <p>At the joint between the arch and the middle leg on the west side cave, a through crack appeared and extended to the inner cave by 1000 mm.</p>	<p>There are several diagonal cracks perpendicular to the arch axis on the cave spandrel of west side cave and middle cave.</p> <p>The crack of the arch vault on the west side cave is connected to the crack of the cave top. The cracks at the arch foot and arch vault of the west cave extend to the back wall.</p> <p>The cracks of the arch vault on the east side cave are connected with the two cracks on the east wall, and the cracks on the vault are vertically connected to the cave top.</p> <p>A slight leaning has been emerged on the middle legs.</p>
East wall	No visible damage	<p>At the top of the wall, a small horizontal crack appeared.</p> <p>At a distance of 500 mm from the north edge and 200 mm from the bottom, a 20 mm long diagonal crack appeared.</p>	<p>The cracks on the cave top continued to extend, and horizontal cracks appeared on both sides of the wall.</p>	<p>A parabola-shaped crack appeared in the upper part of the wall, and the horizontal crack that appeared at the same time was connected to the herringbone crack near the south side of the cave.</p> <p>There is a horizontal crack at the connection between the bottom of the wall and the foundation.</p>

Facade	DL1	DL2	DL3	DL4
West wall	No visible damage	At a distance of 400 mm from the top of the wall, a 500 mm long horizontal crack appeared. At the bottom of the wall 500 mm from the north edge, a 360 mm long horizontal crack appeared.	At the top of the west side wall 400 mm down, a long horizontal crack appeared. At the top of the wall near the south edge, a 120 mm long diagonal crack appeared.	The crack in the middle of the wall communicates with the cracks on the cave top of the southwest and southeast caves and forms a parabolic connection crack. There is a horizontal crack at the connection between the wall and the foundation, and there are signs of sliding.
Global	The specimen is not damaged. Governed by the South wall.	Maximum demand with minor structure damage. Hairline cracks appeared at the edges of the structure, and the overall structure has not been significantly damaged. Governed by the North and South walls.	Maximum demand with moderate structure damage. Governed by the North and South walls.	Maximum demand with heavy structure damage before reaching near-collapse conditions. Governed by the North and South walls.

Due to the whiplash effect, the movement of the top of the structure was more intense, resulting in cracks first generally appearing in the cave roof. It could be found by observing the location where the cracks were concentrated, the damage of the north wall (seen from the south as the back wall in the cave) was mostly concentrated near the east and west edges, and there were long continuous cracks from top to bottom; however, the location of the middle cave had been less damaged, only a slight X-shaped shear crack appeared in the cave and not penetration. Because of the torsional effect of the structure, the farther away from the center axis, the more considerable damage occurred under the action of seismic loads. Some minor slip cracks were observed at the connection between the bottom of the structure and the structure, indicating that the bottom of the cave leg was well connected to the foundation during the loading process, and no apparent slip occurred. The damage of the cave leg itself was relatively light. Still, several horizontal cracks were appeared at the joint between the cave leg and the arch foot, especially the position of the middle cave leg, which was also caused by the uneven distribution of vertical stiffness. Tensile cracks perpendicular to the arch axis also appeared in varying degrees at the above arch. Due to the difference in dynamic response to seismic loading on both sides of the arch foot, led to the tensile stress generated above the arch. The failure of the east and west side wall was relative lightly, and the cracks were concentrated in the upper half of the wall, which was due to the external leaning effect around the Y-axis caused by the earthquake in the X direction and the influence of the artificial mass above the structure. By analyzing the final damage form of the specimen, the weak positions of the stone cave structure are concentrated in the vault, internal wall, and back wall. When the SMLCs are protected in the future, the strength of these weak locations should be increased so that the structure will not be severely damaged or even collapsed under the action of earthquakes. Loaded to $PGA = 0.8 g$, the crack width of the test piece increased significantly, the strength loss of the masonry units was severe, and the specimen reached a critical damage level (DL4) (Fig. 7).

3.2 Dynamic characteristics

Dynamic characteristics are inherent properties of the structure itself, and changes in dynamic characteristics such as natural frequency (ω) and damping ratio (ζ) can reflect changes in the stiffness of the structure before and after loading (Preciado et al. 2019; Pelà et al. 2013). After loading each PGA, frequency-sweep with white noise obtained the natural frequency of the model, and used the half-power bandwidth calculation method to achieve the model damping ratio. The natural vibration frequency and damping ratio of the X- and Y-direction of the structure obtained by the white noise processing at various levels are shown in Fig. 8.

The natural vibration frequency of the X-direction and Y-direction decreased with the increasing of the loading level (PGA), as shown in Fig. 8(a). This was due to the continuous accumulation of structural damage during the step-by-step loading of the model, which led to the gradual decrease of the model structure stiffness. In the initial state of the structure, the initial natural frequency and stiffness in the X direction were more significant than in the Y direction. After loading, the X- and Y-direction natural frequencies decreased to 50.54% and 29.92% of the initial state, respectively, indicating that the X-direction suffered more damage from earthquakes than the Y-direction. With the increase of seismic peak acceleration, the damping ratio of X-direction and Y-direction structures increased (Fig. 8(b)), and with the accumulation of damage, cracks were generated inside the model structure, and the cracks between the model structure foundation and the base gradually development. As the friction energy consumption of the model structure increased, the damping ratio of the structure increased. In the initial state, the Y-direction damping ratio was 3.7 times that of the X-direction damping ratio, indicating that under earthquake action, the X-direction vibration was more robust, and the speed of Y-direction structural attenuation was faster. Compared with the damping ratio before loading, the amplitude of the Y-direction damping ratio change (87.93%) after loading was much smaller than the X-direction (370.15%) damping ratio change. It could be inferred that the structural damage was mainly concentrated in the X-direction.

3.3 Seismic response

(1) Acceleration response

The acceleration amplification factor β is often used to reflect the dynamic response of building structure, and its value is the ratio of the value of the peak response of the structure to the input peak ground acceleration. The input peak ground acceleration adopted the measured value of the acceleration sensor (A23x, A24y, A25z) placed on the ground beam. The peak response acceleration of each crucial part of the stone cave structure taken the maximum value in a single direction (X or Y), two directions (XY), three directions (XYZ). Overall, the acceleration response regularity of stone cave structure under the three seismic waves was very close, and the structural response under the EL wave was relatively large, so in the subsequent analysis, the EL wave was used as an example for detailed analysis. In X and Y direction, the study of dynamic amplification factor under the EL wave taken into PGA of 0.07 g (Frequent earthquake of 7-degree), 0.20 g (Fortification earthquake of 7-degree), 0.44 g (Rare earthquake of 7 degrees and fortification earthquake of 8 degrees), 0.80 g (Rare earthquake of 8 degrees) as examples, and the acceleration amplification factor of critical parts of stone cave is shown in Fig. 9.

For the X-direction, the acceleration amplification factor at the vault of section B-B was smaller than that at the vault of section A-A, because the back wall had a limiting effect on the acceleration response of its adjacent vault. Because the width of the external wall was more significant than that of the internal wall, it had a higher resistance to lateral displacement stiffness, so that the acceleration amplification factor was smaller. Before the fortification intensity (PGA = 0.44 g), the amplified response at the free edge (section A-A) was always higher than at the section B-B of the corresponding member. When the destruction load (0.80 g) was reached, the acceleration amplification factor of the middle cave was significantly reduced. The damage of the external wall was minor due to the larger thickness, and the acceleration amplification factor was not significantly reduced.

Before the fortification intensity (0.20 g), the acceleration response of each part in the Y-direction did not change significantly, but all increased along with the structure height. In particular, the maximum acceleration response of the top of the cave increased by 57.68% compared to the vault, and this gap gradually decreased with the increase of PGA. When the seismic loading reached 0.44 g, the internal wall of the side cave at section A-A was larger than those at section B-B, indicating that the influence of the back wall in the Y-direction was smaller than in the X-direction. The difference between the amplification coefficients of the cave top and the vault was large, and the acceleration coefficient of the cave top gradually decreased with the increase of the PGA. This was the result of the decrease of the structural lateral stiffness (Y direction) caused by damage accumulation.

(2) Displacement response

Take the maximum value of the displacement response of the specimen under different loading conditions for analysis, and the displacement curve envelope is shown in Fig. 10. Overall, the displacement response of the SMLC specimen increased with the increase of the peak ground acceleration of the seismic input. The displacement response below the vault of the specimen increased with the height of the structure, and displacement response of the cave top was smaller than at the vault. When the peak ground acceleration of the specimen was larger ($PGA \geq 0.60$ g), the displacement response of the vault was less than the cave top. The specimen was attained into the plastic state at the $PGA = 0.60$ g, and the crack width was increased, resulting in a redistribution of the stiffness of the specimen and a sudden increase in displacement response of the cave top.

Through investigation, it was found that SMLCs often produced roof fall due to large vertical displacement at the vault, so the displacement response law at the Z-direction of the vault of side and middle cave under each PGA were analyzed. The Z-direction displacement of the vault of the side cave and the middle cave was compared, as shown in Fig. 11. The vertical displacement at the vault of the side and middle caves increased gently before seismic input of $PGA = 0.6$ g, and the difference between the side cave and the middle cave was minor, indicating that there was no visible damage to the vault before $PGA = 0.6$ g. The displacement response of the vault at the Z-direction suddenly increased when $PGA = 0.8$ g, and this moment, the vault had failed, and the roof occurred collapse phenomenon. Also, the middle cave was more severe than the side cave.

3.4 Hysteretic Energy Dissipation

Due to the large seismic response at X-direction under the earthquake action, the X-direction was also the primary energy dissipation direction of the independent stone cave. Therefore, the energy dissipation at X-direction of the specimen under different peak ground accelerations was analyzed. From Fig. 12, as the PGA increasing, the energy consumption of the stone cave structure also gradually increased. When the input peak ground acceleration (El Centro) was 0.14 g, 0.20 g, 0.44 g, the relation curve between the displacement and shear force at the cave top were linearly distributed, and the stone cave specimen was in the elastic stage. After $PGA = 0.60$ g, the stone cave structure produced some irregular shape, and the energy consumption of the structure increased significantly.

The area enclosed by the load-displacement hysteresis curve of the structure represents the energy consumed by the stone cave structure. Used the approximate algorithm obtained the energy consumption of the specimen structure, that is, used the number of sampling points approximated the curve as a straight line within a specific time, and calculated the area, and get the energy consumption. The cumulative energy consumption of the whole structure is calculated as follows,

$$E_{jk}(t_i) = \sum_{i=1}^m \frac{1}{2} [V(t_i) + V(t_{i-1})] [x(t_i) - x(t_{i-1})] \quad (9)$$

where $E_{jk}(t_i)$ is the cumulative energy consumption at the corresponding time t_i under the j -th loading condition; V is the shear force; x is the displacement; m is the total number of samples.

Taking the El Centro wave as an example, the cumulative energy consumption curve of the SMLC under the action of different peak ground accelerations was calculated and plotted, as shown in Fig. 13. With the gradual increase of the peak ground acceleration of the seismic input, the energy dissipation of the structure gradually increased. Because the structural damage gradually intensified and the damage gradually accumulated, so that the hysteretic energy dissipation curve of the structure gradually increased with time and exhibited a step-like rise. Under the fortification earthquake (PGA = 0.2 g), the energy dissipation of the stone cave structure was mainly elastic deformation, especially after $\text{PGA} \geq 0.60$ g, the energy dissipation of the structure was primarily plastic deformation, and the energy dissipation of the structure due to the accumulation of damage sharply increased in a short time.

4 Seismic Evaluation Of The Prototype

Taking into account the recommendations of Kallioras et al. (2018), the damage state (DS) and damage limit (DL) of SMLCs was established. They were linked to the structural response parameters and the test failure phenomena. These five damage states were considered in SMLC: no damage (DS1); minor damage (DS2); moderate damage (DS3); severe damage (DS4); collapse (DS5) (Kallioras et al. 2018; Lagomarsino et al. 2015; Brando et al. 2017). Defining DL(n) as the threshold between DS(n) and DS($n + 1$), there are four damage limits: Limit conditions without visible structural damage (DL1); Limit conditions slight structural damage (DL2); limit conditions moderate structural damage (DL3); limit conditions severe structural damage, before collapse (DL4). The maximum story drift response of the structure after input acceleration was taken as the parameter corresponding to DL(i), which is associated with the last input acceleration peak that caused damage, called DS(i).

Figure 14 summarizes the seismic performance of the SMLC prototype in multiple shaking table tests and gathers some mainly seismic response of the SMLC structure of this test. The displacement response calculated based on the maximum interlayer displacement angle of each structural layer shows that when $\text{PGA} \leq 0.14$ g, the interlayer displacement angle of each structural layer was very close, and then reached DL2. In particular, the range of displacement response of the cave legs was minor. When reached DL3 and DL4 (PGA 0.44 g – 0.80 g), the story drift also increased as the height increases, and the displacement of the cave top increased significantly after $\text{PGA} \geq 0.6$ g, reaching 107.68 mm at DL3.

Before DL1, the acceleration response of the structure was more amplified by the higher structure layer, and the magnification factor of the cave top was 1.24 times that of the cave leg layer. From the EL input, when the damage limit exceeded DL2 (PGA = 0.44 g), the acceleration magnification factor of the arch layer showed a downward trend with PGA increasing. Similarly, the acceleration magnification factor on the cave top had been decreasing with the increase of PGA. After the DL3, the decline rate increased significantly. When reaching DL4, the acceleration magnification factor of the structure was inversely proportional to the height of the structure, and the magnification factor at the cave leg layer was as much as 1.1 times at the cave top layer. Since most of the cave legs were composed of stone masonry without loess, the damage was small during the entire loading process, and the acceleration response continues to rise with the increase of PGA. The loess accounts for 84% of the cross-sectional area of the cave top layer, which caused the vibration damage of the loess to be directly reflected in the acceleration response of the cave top layer. So that the acceleration response of the cave top layer dropped sharply at the beginning to a smooth decline at the later, this results in the acceleration magnification factor gradually decreased after entering the inelastic response range.

With the increase of seismic intensity and damage degree, the basic vibration period of the building aggregate prototype gradually extended from 0.154 s to 0.236 s. After DL1 (PGA = 0.14 g), the first significant change of the period was 0.167 s when PGA = 0.2 g. In DL3 (PGA = 0.44 g), the period was extended to 0.1821 s. The period of the prototype in DL4 (PGA = 0.8 g) was 0.236 s, which was 1.5 times larger than the period of the SMLC structure before loading (0.154 s).

The torsion angle at the vault of the middle cave with the largest displacement response under the action of the X-direction El Centro wave was analyzed. The torsion angle of the structure increased with the increase of the peak ground acceleration. The maximum torsion angle of the stone cave structure was 0.0005 rad under frequent earthquakes (PGA = 0.07 g), and the torsion angle reached 0.0037 rad under the action of destruction earthquake (PGA = 0.8 g). The torsion angle of the structure before the step of the fortification earthquake had a small change range, and the maximum torsion angle not exceeded 0.0014 rad, indicating that the structure was slightly damaged and the torsional stiffness decreases less. After entering the Elasto-plastic stage and the plastic stage, the torsion angle changed significantly (more than 0.001 rad), indicating that the torsional rigidity of the structure decreased when the crack developed and failure degree addition.

In summary, the SMLC in the 7-degree fortification zone had not suffered visible damage (DL2) under the action of rare earthquakes, so it generally not required seismic strengthening treatment. However, for the SMLC in an 8-degree fortification zone, the structure reached DL3 after the action of the fortification earthquake, and there was a risk of collapse at any time under rare earthquakes (DL4). Therefore, the SMLC in the 8-degree fortification zone needed to be strengthened and reconstructed in the weak parts to prevent their severe damage or even collapse under the action of the earthquake.

5 Summary And Concluding Remarks

- The SMLC had excellent aseismic performance, and under the action of a 7-degree rare earthquake (PGA = 0.22 g), the seismic performance of the structure had not decreased significantly, and the damage was minor. The destruction of SMLC was mainly caused by cracking of mortar joints, and the failure was primarily concentrated on the vault and internal wall on the free side (section A-A), so it was a weak part of the SMLC. Some slippage phenomenon had appeared between the bottom of the cave leg and the foundation, so the middle cave leg and the foundation needed to strength the reliable connection.
- As the PGA of the input seismic wave increasing, the natural frequency of the SMLC structure decreased, and the damping ratio increased. The acceleration response of the specimen structure increased with the rise of the PGA and gradually increased along the height direction of the structure. The acceleration response of the vault at the free edge (section A-A) was higher than that at the back wall, indicating that the back wall had a strong constraint on the vault.
- The horizontal displacement of each part of the SMLC was subjected to linearly similar forced vibration according to the time-history curve of the basic excitation feedback, and the structural displacement response increased with the increase of the PGA. After the structure exceeded the 7-degree rare earthquake action (DL2), the maximum lateral displacement was transferred from the vault to the cave top, and the maximum lateral displacement angle was 1/102. When the PGA reached an 8-degree rare earthquake action (DL4), the roof fall appeared in the SMLC, and the side cave was more dangerous.
- The stiffness of the SMLC structure was severely eccentric, and the torsional response of the specimen structure under the earthquake action increased with the PGA increasing. The torsion angle when reaching DL4 was 7.4

times greater than that of DL2, indicating that the torsional effect of the structure had a more significant impact on the seismic performance of the SMLC.

- As the PGA increasing, the area enclosed by the load-displacement hysteresis curve of the overall structure of the SMLC continuously increased, indicating that the energy consumption of the structure continues to grow and at the same time the overall rigidity of the structure shown a gradual downward trend, indicating that the damage of the structure is gradually accumulating.
- The SMLC buildings in the 8-degree fortification zone needed to be evaluated for seismic performance, and the weak areas should be strengthened. If no visible damage appeared to the SMLC buildings in the 7-degree fortification zone, no treatment is required.

Declarations

Authors Contribution Conceptualization, X.B. Zhao and J.Y. Xue; methodology, X.B. Zhao, F.L Zhang and J.Y. Xue; formal analysis, X.B. Zhao; investigation, F.L Zhang and J.Y. Xue; resources, X.B. Zhao, F.L Zhang and J.Y. Xue; writing-original draft preparation, X.B. Zhao; writing-review and editing, F.L Zhang and J.Y. Xue; visualization, F.L Zhang and J.Y. Xue; project administration, F.L Zhang; funding acquisition, J.Y. Xue. All authors have read and agreed to the published version of the manuscript.

Funding The authors would like to thank the National Natural Science Foundation of China (51608435), Shaanxi Key Scientific and Techno-logical Innovation Team Project (2019TD-029), and Shaanxi S&T Co-ordinate Innovation Project (2016KTZDSF04-04), Shaanxi Province of Housing and Urban-rural Development Science and Technology Plan Project (2019-K24) and Shaanxi Innovation Talent Promotion Plan (2019KJXX-018).

Data availability The free vibration test data used to support the findings of this study are available from the corresponding author upon request.

Conflicts of interest The authors declare that they have no conflict of interest.

References

1. Aktas YD, Turer A (2016) Seismic performance evaluation of traditional timber HA plus /-mA plus /-AY frames: capacity spectrum method based assessment. *Bull Earthq Eng* 14(11):3175–3194
2. Ballard L, Rudofsky B, Ransom HS, Mumford L, Deutsch KW (1967) Architecture without architects. *Journal of Aesthetics Art Criticism* 25:226
3. Bennati S, Salvatore W, Nardini L (2015) Dynamic behavior of a medieval masonry bell tower. Part I: experimental measurements and modeling of bell's dynamic actions. *J Struct Eng* 131:1647–1655
4. Borri A, Corradi M, Castori G, De Maria A (2015) A method for the analysis and classification of historic masonry. *Bull Earthq Eng* 13(9):2647–2665
5. Brando G, De Matteis G, Spacone E (2017) Predictive model for the seismic vulnerability assessment of small historic centres: application to the inner Abruzzi Region in Italy. *Eng Struct* 153:81–96
6. Cakir F, Uckan E, Shen J, Seker S, Akbas B (2016) Seismic performance evaluation of slender masonry towers: a case study. *Struct Des Tall Specif Build* 25(4):193–212
7. Carocci CF (2012) Small centres damaged by 2009 L'Aquila earthquake: on site analyses of historical masonry aggregates. *Bull Earthq Eng* 10(1):45–71

8. Colapietro D, Fiore A, Netti A, Fatiguso F, Amarano GC, Fino MD, Cascella D, Ancona A (2013) Dynamic identification and evaluation of the seismic safety of a masonry bell tower in the south of Italy. *Int Conf Comput Methods Struct Dyn Earthq Eng* 12–14 June 2013, Kos Island, Greece
9. Corradi M, Borri A (2018) A database of the structural behavior of masonry in shear. *Bull Earthq Eng* 16(9):3905–3930
10. Costa AA, Arede A, Costa A, Guedes J, Silva B (2012) Experimental testing, numerical modelling and seismic strengthening of traditional stone masonry: comprehensive study of a real Azorian pier. *Bull Earthq Eng* 10(1):135–159
11. D’Ayala DF, Paganoni S (2011) Assessment and analysis of damage in L’Aquila historic city centre after 6th April 2009. *Bull Earthq Eng* 9(1):81–104
12. ENV 1996-1-1 (2005) C.E. de Normalisation, Eurocode 6: Design of Masonry Structures-Part 1–1: General Rules for Reinforced and Unreinforced Masonry Structures. Comit Europeen de Normalisation, Brussels
13. Ersoy HY (2001) Composite Material. Literature, Istanbul, Turkey
14. GB 50003 – 2011 (2011) Code for design of masonry structures [S]. China Architecture & Building Press, China (in Chinese)
15. GB 50011 – 2010 (2016) Code for seismic design of buildings [S]. China Architecture & Building Press, China (in Chinese)
16. GB/T 50266 – 2013 (2013) Standard for test methods of Engineering Rock Mass [S]. China Planning Press, China (in Chinese)
17. Graziotti F, Tomassetti U, Kallioras S, Penna A, Magenes G (2017) Shaking table test on a full scale URM cavity wall building. *Bull Earthq Eng* 15(12):5329–5364
18. Hendry AW, Khalaf FM (2001) Masonry Wall Construction. Spon Press, London
19. JGJ/T 136–2017 (2017) Technical Specification for Testing the Compressive Strength of Masonry Mortar by Penetration Method Resistance Method [S]. China Architecture & Building Press, China (in Chinese)
20. JGJ/T 70-2009 (2009) Standard for Test Method of Performance on Building Mortar [S]. China Architecture & Building Press, China (in Chinese)
21. Kahraman S, Fener M, Kozman E (2012) Predicting the compressive and tensile strength of rocks from indentation hardness index. *J South Afr Inst Min Metall* 112(5):331–339
22. Kallioras S, Guerrini G, Tomassetti U, Marchesi B, Penna A, Graziotti F, Magenes G (2018) Experimental seismic performance of a full-scale unreinforced clay-masonry building with flexible timberdiaphragms. *Eng Struct* 161:231–249
23. Krzan M, Gostic S, Cattari S, Bosiljkov V (2015) Acquiring reference parameters of masonry for the structural performance analysis of historical buildings. *Bull Earthq Eng* 13(1):203–236
24. Lagomarsino S, Cattari S (2015) PERPETUATE guidelines for seismic performance-based assessment of cultural heritage masonry structures. *Bull Earthq Eng* 13(1):13–47
25. Lagomarsino S, Penna A, Galasco A, Cattari S (2013) TREMURI program: An equivalent frame model for the nonlinear seismic analysis of masonry buildings. *Eng Struct* 56:1787–1799
26. Magenes G, Penna A, Senaldi IE, Rota M, Galasco A (2014) Shaking table test of a strengthened fullscale stone masonry building with flexible diaphragms. *Int J Archit Herit* 8(3):349–375
27. Milosevic J, Gago AS, Lopes M, Bento R (2013) Experimental assessment of shear strength parameters on rubble stone masonry specimens. *Constr Build Mater* 47:1372–1380

28. MIT (2009) Ministry of Infrastructures and Transportation, Circ. N. 617 of 2/2/ 2009: Istruzioni per l'applicazione delle nuove norme tecniche per le costruzioni di cui al Decreto Ministeriale 14 Gennaio 2008, Italy
29. Mouzakis C, Adami CE, Karapitta L, Vintzileou E (2018) Seismic behaviour of timber-laced stone masonry buildings before and after interventions: shaking table tests on a two-storey masonry model. *Bull Earthq Eng* 16(2):803–829
30. Pelà L, Aprile A, Benedetti A (2013) Comparison of seismic assessment procedures for masonry arch bridges. *Constr Build Mater* 38:381–394
31. Poletti E, Vasconcelos G (2015) Seismic behaviour of traditional timber frame walls: experimental results on unreinforced walls. *Bull Earthq Eng* 13(3):885–916
32. Preciado A (2015) Seismic vulnerability and failure modes simulation of ancient masonry towers by validated virtual finite element models. *Eng Fail Anal* 57:72–87
33. Preciado A, Sperbeck ST (2019) Failure analysis and performance of compact and slender carved stone walls under compression and seismic loading by the FEM approach. *Eng Fail Anal* 96:508–524
34. Proske D, Gelder P (2009) *Safety of Historical Arch Bridges*. Springer-Verlag, Heidelberg Dordrecht
35. Ril 805 (1999) Richtlinie 805: Tragsicherheit bestehender Eisenbahnbrücken. DB Netz AG 2002
36. Rovero L, Alecci V, Mechelli J, Tonietti U, De Stefano M (2016) Masonry walls with irregular texture of L'Aquila (Italy) seismic area: validation of a method for the evaluation of masonry quality. *Mater Struct* 49(6):2297–2314
37. Senaldi I, Guerrini G, Scherini S, Morganti S, Magenes G, Beyer K, Penna A (2018) A Natural stone masonry characterization for the shaking-table test of a scaled building specimen. In: *Proceedings of the 10th international masonry conference, Milan, Italy*
38. Siegesmund S, Snethlage R (2011) *Stone in Architecture: Properties. Durability*, Springer
39. Silva B, Dalla BM, da Porto F, Modena C (2014) Experimental assessment of in-plane behaviour of three-leaf stone masonry walls. *Constr Build Mater* 53:149–161
40. Tomassetti U, Correia AA, Marques A, Graziotti F, Penna A, Magenes G (2017) Dynamic collapse testing of a full-scale URM cavity-wall structure. *Proceedings of the XVII ANIDIS conference, Pistoia, Italy*
41. Tomaževic M, Weiss P, Velechovsky T (1991) The influence of rigidity of floors on the seismic behavior of old stone-masonry buildings. *Eur Earthq Eng* 3:28–41
42. Valente M, Milani G (2016) Seismic assessment of historical masonry towers by means of simplified approaches and standard FEM. *Constr Build Mater* 108:74–104
43. Vasconcelos G, Lourenço PB, Alves CAS, Pamplona J (2009) Compressive Behavior of Granite: Experimental Approach. *J Mater Civil Eng* 21:502–511
44. Vintzileou E, Mouzakis C, Adami CE, Karapitta L (2015) Seismic behavior of three-leaf stone masonry buildings before and after interventions: shaking table tests on a two-storey masonry model. *Bull Earthq Eng* 13(10):3107–3133
45. Xie QF, Wang L, Li SY, Zhang LP, Hu WB (2020a) Influence of wood infill walls on the seismic performance of Chinese traditional timber structure by shaking table tests. *Bull Earthq Eng* 18(10):5009–5029
46. Xie QF, Wang L, Zhang LP, Hu WB, Zhou TG (2019) Seismic behaviour of a traditional timber structure: shaking table tests, energy dissipation mechanism and damage assessment model. *Bull Earthq Eng* 17(3):1689–1714
47. Xie QF, Xu DF, Zhang Y, Yu YW, Hao WP (2020b) Shaking table testing and numerical simulation of the seismic response of a typical China ancient masonry tower. *Bull Earthq Eng* 18(1):331–355
48. Xue JY, Zhao XB, Zhang FL, Xu D, Hu XF, Ma LL (2020) Shaking table tests on seismic behavior of the underground loess cave of earth building of traditional dwellings. *Eng Struct* 207:110221

49. Yu CL, Zhao FH (2009) The Ecological Measures of the New Type of Cave Dwelling Design in Loess Plateau. Int Conf Inf Manag 2:203–206
50. Zhao XB, Xue JY, Zhang FL, Hu XF, Zhang X, Xu D (2020) Investigation of numerical analysis and seismic performance of underground loess cave with traditional dwellings. Soil Dyn Earthq Eng 140:106426
51. Zhao XB, Xue JY, Zhang FL, Liu XH, Luo Z, Ma LL, Zhang W (2021) Aseismic retrofitting of loess cave using composite materials by shaking table test. Compos struct 268:113965
52. Zhao XB, Zhang FL, Xue JY, Ma LL (2019) Shaking table tests on seismic behavior of ancient timber structure reinforced with CFRP sheet. Eng Struct 197:109405
53. Zhang S, Beyer K (2019) Numerical investigation of the role of masonry typology on shear strength. Eng Struct 192:86–102
54. Zhang S, Hofmann M, Beyer K (2018) A 2D typology generator for historical masonry elements. Constr Build Mater 184:440–453
55. Zhu XR, Liu JP, Liu Y, Hu RR (2014) Energy performance of a new Yaodong dwelling, in the Loess Plateau of China. Energ Build 70:159–166

Figures

Figure 1

Stone masonry loess cave

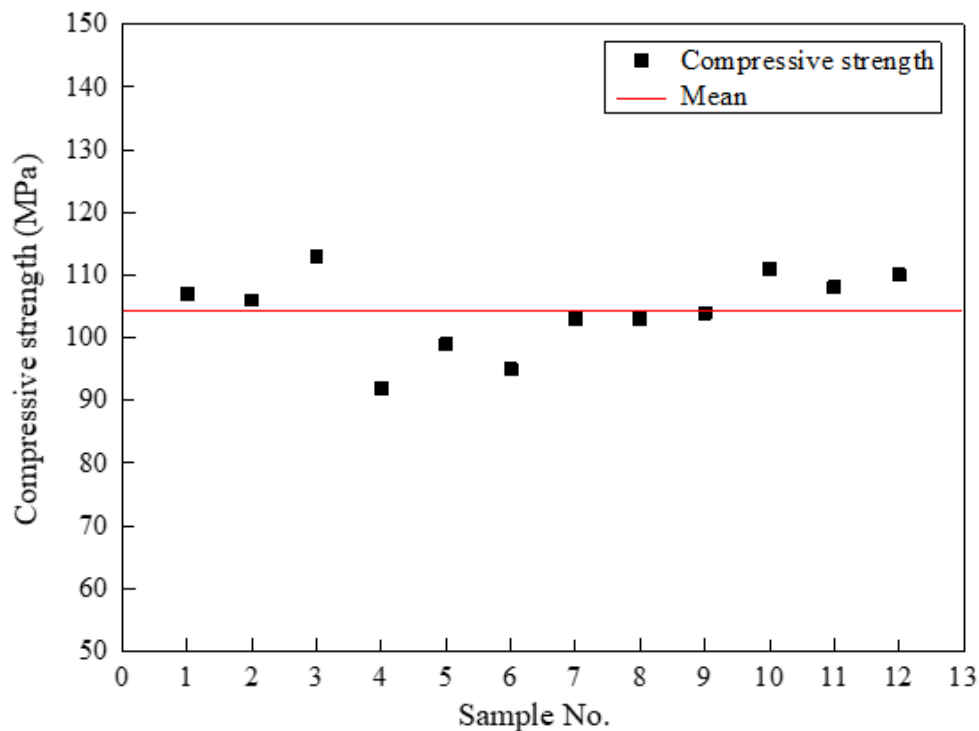


Figure 2

Discrete diagram of stone compressive strength

Figure 3

Stone masonry loess cave configuration: (a,b) main material; (c) first floor; (d) cave leg; (e) arch; (f) stonework completed; (g) infilled loess; (h) specimen construction completed

Figure 4

Arrangement of displacement and acceleration sensors on each layer. Note: The red rectangle represents the displacement meter, and the blue circle represents the accelerometer. In addition, x, y, and z represent the measurement direction respectively.

Figure 5

Acceleration records and Fourier spectra of the input motions on the shaking table. (a) EL Centro, (b) LA – Hollywood, (c) Artificial and (d) Response spectrum curve.

Figure 7

Observed failure at the end of test (PGA=0.8 g)

Figure 8

The natural frequency and damping ratio of SMLC in two directions

Figure 9

The acceleration magnification factor along the height of stone masonry loess cave under each PGA Note: the leg on the side cave represents the external wall of the cave, and the leg on the middle cave represents the internal wall of the cave.

Figure 10

Displacement envelope under different seismic inputs

Figure 11

The displacement of Z-direction on vault

Figure 12

Hysteretic curve of force vs. displacement on X-dir.

Figure 13

The cumulative energy consumption curve of the whole structure under EL input

Figure 14

Summary of the prototype performance